Наносистеми, наноматеріали, нанотехнології
Nanosistemi, Nanomateriali, Nanotehnologii
2024, т. 22, № 3, сс. 739–768
https://doi.org/10.15407/nnn.22.03.739

PACS numbers: 68.37.Hk, 68.37.Ps, 68.37.Vj, 73.50.Pz, 78.30.Na, 81.07.-b, 88.40.hj

Low-Cost TiO_2/MWCNT/Ag Dye-Sensitized Solar Cell Based on Polypyrrole/SDS Counter Electrode

Nuhad Saad and Oraas Adnan

College of Science,
Department of Chemistry,
University of Al-Qadisiyah
Al Diwaniyah, Al-Qadisiyah, Iraq

In this study, titanium dioxide/multiwall carbon nanotube and silver nanoparticles (TiO_2/MWCNTs/Ag) nanocomposite is employed as photoanode incorporated with polypyrrole/sodium dodecyl sulphate (PPy + SDS) counter electrode 1 (C_1) and polypyrrole/sodium dodecyl sulphate/multiwall carbon nanotube (PPy + SDS + MWCNT) counter electrode 2 (C_2) as low-cost counter electrodes compared with a platinum counter electrode to construct dye-sensitized solar cells (DSSCs) using Ru-based dyes Z907, pomegranate dye, arugula dye, and hibiscus dye as a photosensitized one. The working electrode composite is deposited on a transparent-conducting $F:SnO_2$ (FTO) glass substrate by a thermal chemical spraying technique and, then, anchored with dyes, while the counter electrodes are prepared by the electropolymerization method. The structural and optical properties and interconnectivity of the materials within the composite are investigated thoroughly through various characterization techniques x-ray diffraction (XRD), Raman scattering, field-emission scanning electron microscopy (FESEM), and atomic force microscopy (AFM). Finally, the photovoltaic performances of the assembled DSSCs are tested under photoirradiation (100 mW/cm^2). The measured current–voltage (I–V) curve shows that the efficiency of DSSCs in the case of Z907 dye with C_1 and C_2 is of 2.537% and 2.453%, respectively, compared with the reference cell based on the Pt counter electrode, which has an efficiency of 3.57%, that indicates a good efficiency of the low-cost prepared DSSCs. The natural dyes exhibit a moderate efficiency ranging from 1.44–0.53%.

У цьому дослідженні нанокомпозит діоксид Титану/багатошарові вуглецеві нанотрубки та наночастинки срібла (TiO_2/MWCNTs/Ag) використовували як фотоаноду, об'єднану з протиелектродою 1 (C_1) поліпірол/додецилсульфат натрію (PPy + SDS) та протиелектродою 2 (C_2) поліпірол/додецилсульфат натрію/багатостінні вуглецеві нанотрубки (PPy + SDS + MWCNT) як недорогими протиелектродами порівняно з

платиновою протиелектродою для створення сенсибілізованих до барвника сонячних елементів (DSSCs) з використанням барвника Z907 на основі Ru, ґранатового барвника, барвника-руколи, барвника-гібіскусу як фотосенсибілізаторів. Робочий електродний композит був нанесений на прозору провідну скляну підкладинку з F:SnO_2 (FTO) методом термічного хемічного напорошення, а потім закріплений барвниками, тоді як протиелектроди були підготовлені методом електрополімеризації. Структурні й оптичні властивості та взаємозв'язок матеріялів у складі композиту ретельно досліджено за допомогою різних методів визначення характеристик рентґенівської дифракції (XRD), комбінаційного розсіяння, польової емісійної сканувальної електронної мікроскопії (FESEM) та атомно-силової мікроскопії (AFM). Нарешті, фотоелектричні характеристики зібраних DSSCs було перевірено під дією фотоопромінення (100 мВт/см^2). Виміряна вольт-амперна крива (I–V) показує, що ефективність DSSCs у випадку барвника Z907 з C_1 і C_2 становила 2,537% і 2,453% відповідно порівняно з еталонною коміркою на основі Pt-протиелектроди, яка має ефективність у 3,57%, а це свідчить про хорошу ефективність недорогих виготовлених DSSCs. Натуральні барвники показали помірну ефективність у межах 1,44–0,53%.

Key words: TiO_2, silver nanoparticles, MWCNT, Z907, SDS, PPy, dye-sensitized solar cell.

Ключові слова: TiO_2, наночастинки срібла, MWCNT, Z907, SDS, PPy, сенсибілізований до барвника сонячний елемент.

(Received 20 July, 2023; in revised form, 26 July, 2023)

1. INTRODUCTION

Due to its low cost, simple manufacturing process, and greener design, dye-sensitized solar cells (DSSCs) have undergone extensive research as a substitute energy source. A DSSC is made up of a glass substrate covered with a transparent conducting oxide layer, an electron-transporting mesoporous metal oxide layer, dye, electrolyte, and a counter electrode. Generally, the spectral sensitization of wide bandgap semiconductors like TiO_2 is used in DSSCs to convert visible light into electricity,TiO_2 continues to be the most promising semiconductor discovered so far for DSSCs [1]. Natural dyes employed in DSSC as sensitizers are less expensive than synthetic dyes, although their stated efficiencies are fairly poor [2]. Tennakone *et al.* first proposed the idea of a dye-sensitized solid-state solar cell in 1988, and later O'Regan and Grätzel reported an efficiency of 7.1% and a current density greater than 12 mA·cm^2 for DSSC in which I^{-3}/I^{-} redox couple and TiO_2 were used as liquid electrolytes, respectively.

Nazeeruddin *et al.* later reported the maximum efficiency of

11.1% [3].

The performance of DSSCs is nonetheless hampered by the relaxation of oxidized dye and recombination processes linked to the charge carriers. Utilizing a doped TiO_2 electrode is one of the alternate methods to lessen the aforementioned issue in DSSCs. It is obvious that dopant materials affect features such as conduction band energy, charge transit, recombination, and collection of charge carriers by narrowing the bandgap and increasing the charge traps of TiO_2. While many different dopants, including transition metals, alkali earth metals, non-metals, and rare earth elements, have been used, the incorporation of transition metals into TiO_2 results in the formation of a wide variety of new energy levels because the partially filled *d*-orbitals of transition metals close to the conduction band (CB) are responsible transition metal Ag have been used as dopant in TiO_2 [4].

H. Hwang *et al.* [5] developed the efficiency of TiO_2 Photoanode using the surface plasmonic effect of silver nanoparticles (NPs) and the high electron mobility of CNTs with Pt counter electrode. The TiO_2/CNT composite working electrode with 0.5 wt.% CNTs had increased efficiency over that of the conventional pure TiO_2 working electrode. Finally, a two-fold higher efficiency than the conventional working electrode was achieved by using a TiO_2/Ag/CNT composite working electrode. This greater efficiency may be caused by the synergism between the surface plasmonic effect of the silver nanoparticles and the high electron mobility of the MWCNT network. This cell was use as reference cell in the current study.

As alternative cost-efficient materials, various counter electrode (CE) materials including carbon-based materials, conducting polymers, sulphides, nitrides, and carbides have been integrated into DSSCs.

Polypyrrole (PPy) has attracted much research attention due to its high conductivity, low cost, large electrochemical surface area, and good electrocatalytic activity for I_3-reduction enabling application in electronics, catalysis, energy storage, and sensing [6, 7]. Wu *et al.* [8] have prepared PPy nanoparticles and applied as CE catalyst in DSSC sand got remarkable power conversion efficiency.

The combination of surfactant with polypyrrole tends to be improved the counter electrode properties. Sodium dodecyl sulphate (SDS) surfactant and MWCNT are expecting to achieve better catalytic activity and device performance. Introduction of SDS surfactant additive significantly enhances the photovoltaic performance [9].

At present study and as alternative cost-efficient DSSCs, we attempted to study the effect of merge both Pt/Ag/MWCNT as working electrode and PPy/SDS as counter electrode with different types of dye.

2. MATERIALS AND METHODS

2.1. Materials

All materials and solvents used were obtained from commercial sources: titanium dioxide TiO_2 (97%, PanReac), silver nanoparticles Ag (≥ 99.9%, QSI, Nano), multiwall carbon nanotube MWCNT (98.9%, Sigma Aldirch), ethanol (≥99.8%, Honeywell), pyrrole (99%, Sigma Aldirch), Perchloric acid (99.9%, THOMAS BAKER), sodium dodecyl sulphate SDS (≥99%, Sigma Aldrich), Iodide (≥94%, Sigma Aldirch), potassium iodide (99%, Sigma Aldirch), ethylene glycol (97%, BrcelonaEspan), ruthenium complex dye Z907 (95%, Ossila), tert-butanole (99%, Sigma Aldirch), acetonitrile (99.8%, Sigma Aldrich).

2.2. Methods

2.2.1. Preparation of TiO_2/Ag 2.0 wt.%/MWCNT 0.5 wt.%

The purified MWCNTs were dispersed in ethanol (> 99.9% purity) using a sonicator for 30 min, and the well-dispersed MWCNTs were then separated from the solution by centrifugation for 3 min. Silver nanoparticles (QSI-Nano; > 99.9% purity, 20–40 nm in diameter) and TiO_2 were added to the prepared MWCNTs solution *via* ultrasonication.

Photoanode was fabricated using the prepared TiO_2/Ag/MWCNT composite solution with 140 ml ethanol. Firstly, the prepared TiO_2/Ag/CNT composite solution was spray on a fluorine-doped tin oxide FTO glass substrate using the thermal chemical spraying method then thermally sintered at 500°C for 2 hours, modified [5].

2.2.2. Preparation of Counter Electrodes

Electrochemical polymerization of PPy1 onto FTO glass was carried out in a deionized (DI) water containing 4 drops of perchloric acid ($HClO_4$), 0.1 M pyrrole monomer, 0.1 M sodium dodecyl sulphate (SDS) as an anionic surfactant and by using the potentiostatic method by applying a potential value of 0.8 V for 30 sec.

In the case of PPy1/MWCNT CEs, we used 0.01 g of MWCNT in addition to the previous mixture. Prior to the film deposition, the solution was stirred for 3 h in an ice bath and then purged with nitrogen. A three-electrode system was used with FTO glass as working electrode, Pt sheet as counter electrode, and Ag/AgCl as reference electrode for electrochemical polymerization, modified [9].

2.2.3. Preparation of Pomegranate Dye

In this research, pomegranate extract was used as a dye. This raw material was collected from the local market and washed to reduce the dust particles. The pure juice was extracted by hand grinding method was applied on pomegranate. The extracted dye was filtered through the net and then filter paper to obtain clear dye [10].

2.2.4. Preparation of Hibiscus Leaf Extract Dye Solution

10 g of hibiscus leaves was mixed with 160 ml of deionized water and leave it for a 6hours , Then 10 ml of ethanol and 10 ml of dilute acetic acid were added to the mixture, stirred for an hour at room temperature after which it was filtered [11].

2.2.5. Preparation of the Chlorophyll Dye by Arugula Leaves (Fresh)

60 g of Arugula is crushing using mortar into small size 100 ml of ethanol is added into the Arugula and is placed into the ultrasonic for 30 minutes with the frequency of 37 Hz using Degas mode for extracting chlorophyll process. After that, enter the solvents into a centrifuge for 25 minutes with 5000 rpm [12].

2.2.6. Preparation of Z907 Dye

0.3 mM of Z907 dye was prepared in 1:1 mixture of acetonitrile tert-butanol, where the electrodes are immersed for 20 hours [13].

2.2.7. Preparation of Electrolyte

The iodide solution is prepared by dissolving 0.127 g iodine (I^2) in 10 mL of ethylene glycol to which 0.83 g potassium iodide (KI) is added, stirred and stored in a dark container [14].

2.3. Fabrication of DSSCs

The fluorine-doped tin oxide (FTO) coated conducting glass was used as the current collector. It was cleaned initially with soap water and subsequently with distilled water and ethanol using an ultrasonic bath. Then, the synthesized TiO_2 nanomaterial was made into solution by mixing with silver nanoparticles, multiwall carbon nanotube and ethanol and coated on FTO by the thermal chemical

spraying technique. Then, the coated glasses were soaked in 0.3 mM solution of Z907 dye in acetonitrile/tert-butyl alcohol for 24 h. The dye-coated Ru-doped TiO_2 electrode and Pt counter electrode were used to assemble the cell and I^{-3}/I^{-} electrolyte was used as redox electrolyte.

2.4. Characterization

The structural properties of the synthesized nanomaterials were studied by the x-ray diffraction method. A Raman spectroscopic study was carried out using a laser confocal Raman microscope. The optical absorbance spectra were recorded using DRS spectrophotometer. The elemental composition of the synthesized nanomaterials was analysed by the energy-dispersive x-ray spectroscopy technique. Current–voltage (I–V) characteristics in the illumination were measured as well as surface pours by FESEM. The effective area of the photoelectrode was 0.25 cm^2. Electrochemical impedance spectroscopy (EIS) measurements were carried out on the DSSCs using MetrohmAutolabpotentiostat.

3. RESULTS AND DISCUSSION

3.1. XRD of Films

X-ray diffraction spectroscopy is used to determine some structural properties such as crystalline phase and crystalline size. The crystal size can be calculated by the Debye equation:

$$D = k\lambda / \beta \cos\theta, \tag{1}$$

D is crystal size rate; K—the form factor, whose value is usually 0.9; λ—the wavelength of x-rays, which has a value of 0.154056; β—the total width is half of the greatest height; θ—deviation angle.

Crystal layers are also calculated by Bragg's law:

$$d = n\lambda / \beta \cos\theta, \tag{2}$$

d is the spacing between the crystal planes; n represents an integer (1, 2, 3, ...).

The x-ray diffraction (XRD) pattern of anode (TiO_2, MWCNT and Ag) revealed that the highest peak of MWCNT appeared at 27.33°. Based on the results, it can be concluded that surface functionalization has little effect on the average d-spacing [15]. The strongest diffraction peaks, located at 38.14°, corresponded to anatase TiO_2.

The anatase structure also accounted for the peak at 51.73°, while the peak at 55.44° was attributed to the rutile structure. These results indicate that the primary crystal phase of the TiO_2 nanoparticles was anatase with trace amounts of rutile phases present in the sample. The broad peaks in the XRD pattern indicated that the particles were in the nanometer se range and did not contain any contaminants. The TiO_2 NPs were found to have a tetragonal anatase structure with trigonal planar and octahedral geometry, which is consistent with previous studies in the literature survey [16, 17].

The XRD pattern also shows a prominent peak at 62.02°, indicating the presence of green-synthesized Ag NPs with a face centred

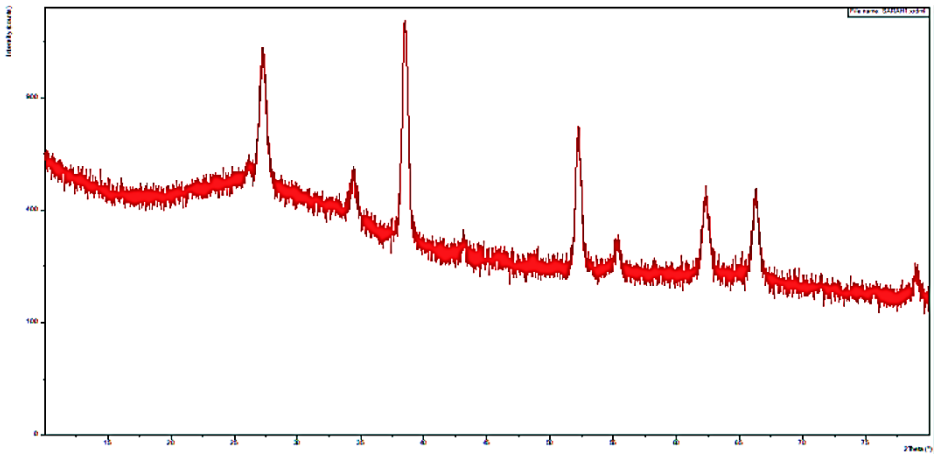

Fig. 1. XRD patterns of photoanode.

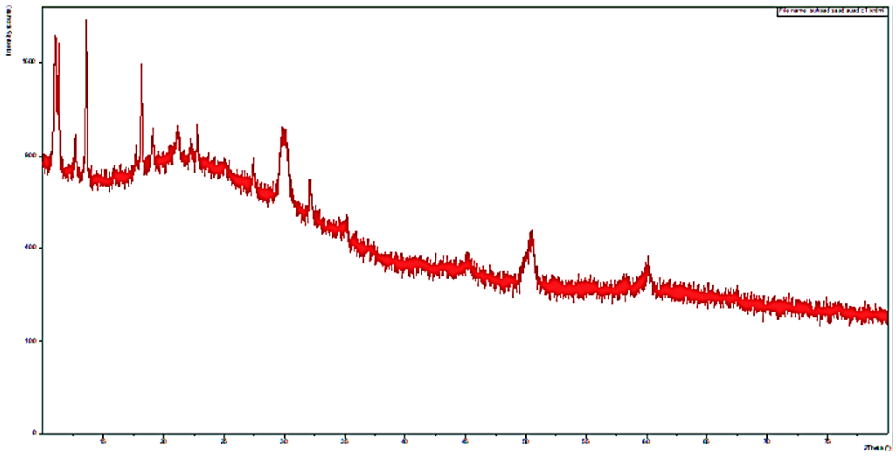

Fig. 2. XRD patterns of Cathode 1.

cubic structure (f.c.c. structure). The average crystalline size of the silver nanoparticles was estimated using the Debye equation [18].

For Cathode 1, the x-ray diffraction patterns revealed the presence of multiple distinct peaks, indicating the presence of SDS as crystalline materials. These peaks were found to have characteristic diffraction angles of 4.5° and 8.9° [19]. On the other hand, the XRD pattern of the PPy exhibited a broad peak at 29.8°, suggesting that it was amorphous in nature [20].

To determine the structural properties of Cathode 2, x-ray diffraction (XRD) analysis was conducted. The XRD pattern showed two peaks at 25° and 45° corresponding to MWCNT a broad peak centred at a characteristic angle, indicating the presence of amorphous carbon material. The most prominent diffraction peak in the

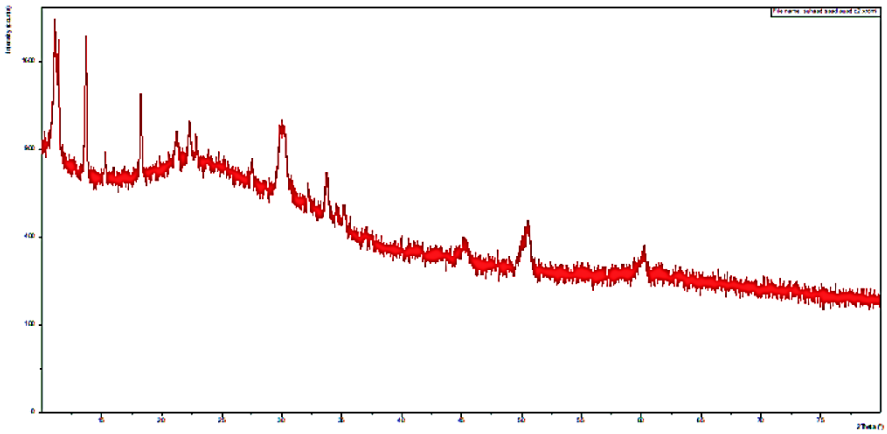

Fig. 3. XRD patterns of Cathode 2.

TABLE 1. X-ray diffraction variables for electrodes.

Compound	2θ, degree	*d*, Å	FWHM	*D*, nm	Intensity *I*/*I*, %
Anode 1 (TiO_2, MWCNT, Ag)	27.3397	3.25947	0.1596	17.9	36
	38.1484	2.35715	0.2112	44	76
	51.7375	2.16237	0.3168	26.3	105
	55.4402	2.03216	0.4224	19	199
	62.0249	1.49508	0.3168	28.9	52
Cathode 1 (PPy, SDS)	29.8069	2.99505	0.1732	57.5	3532
Cathode 2 (PPy, SDS, MWCNT)	35.3015	2.54045	0.2598	37.3	797
	50.6211	1.80177	0.2598	39.3	1628
	32.2251	2.77560	0.1732	57.9	778

XRD pattern of PPy is usually observed around $2\theta = 20°$. This peak corresponds to the interplanar spacing between the polymer chains and is indicative of the degree of ordering in the material. Thus, it can be concluded that the amorphous character of carbon dominates in the MWCNTs/PPy1 nanocomposite. Moreover, the shift in the position of the XRD peaks of the fabricated nanocomposite indicates the successful formation of the MWCNTs/PPy1 nanocomposite [21]. The x-ray diffraction patterns revealed also the presence of multiple distinct peaks, indicating the presence of SDS as crystalline materials. These peaks were found to have characteristic diffraction angles of 4.5° and 8.9° [19].

3.2. Field-Emission Scanning Electron Microscopy (FESEM)

The displayed images in Fig. 4 are FESEM pictures. Raw MWCNTs tend to collect together like bundles due to the van der Waals forces between the tubes. The FESEM pictures of the MWCNTs/TiO_2 and Ag nanocomposites show that the CNTs were linked to semi-spheres of TiO_2/Ag NPs with varying diameters. Chemical oxidation using powerful oxidizing agents led to severe etching of the graphitic surface of the tubes, resulting in a significant number of disordered sites. However, the MWCNTs' structure remained intact even after being coated with TiO_2/Ag NPs, as evidenced by the aforementioned findings. The FESEM pictures at different magnifications revealed the presence of uniformly distributed, spherical nanoparticles of TiO_2/Ag NPs [22].

The typical structure of aggregates is evident on the surface facing the opposing electrode, as depicted in Fig. 5. Despite undergoing several scans, the surface has developed numerous fissures, resulting in an increase in electroactivity due to the increased surface area resulting from the fractures. The polymer surface has degrad-

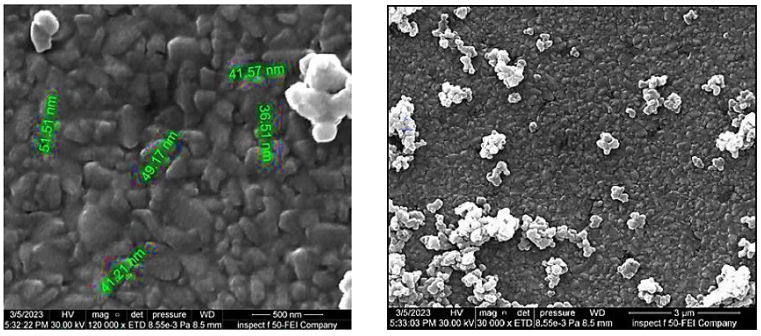

Fig. 4. FESEM images of photoanode.

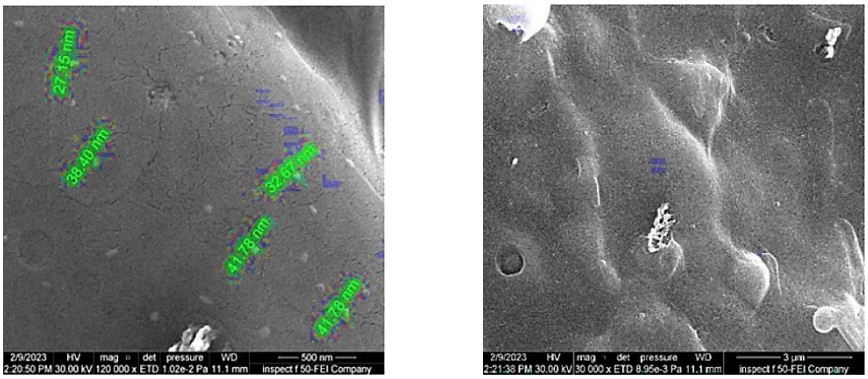

Fig. 5. FESEM images of Cathode 1.

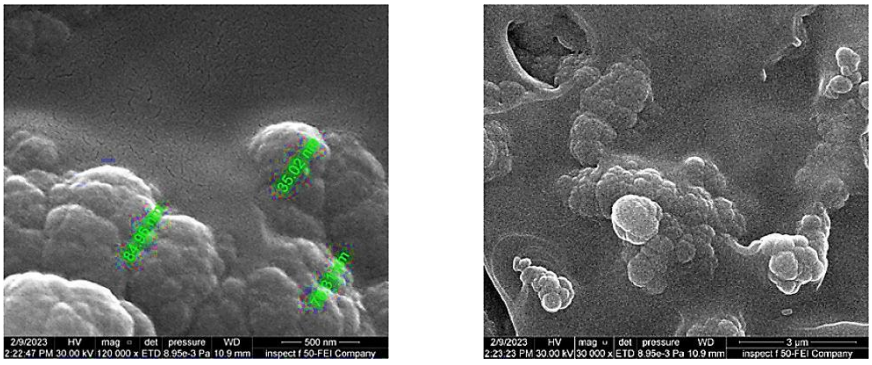

Fig. 6. FESEM images of Cathode 2.

ed, and the extended potential scan has caused the loss of multiple active spots [23].

To investigate further, the surface carbon and oxygen levels of the PPy/SDS–CNT electrodes were measured using FESEM. The cross-sectional FESEM images demonstrate a smoothed-out surface, with a reduced thickness of the PPy/SDS–CNT electrode. Rather than forming a uniform plane enclosing the SDS–CNT micelles, a cauliflower-like structure was formed [24].

3.3. Raman Spectroscopy

Figure 7 displays MWCNTs with complex spectra that can be understood by examining individual components and any potential interactions within the composite. Unmodified MWCNT samples exhibit two distinct peaks at approximately 1451 and 4023 cm^{-1}, with

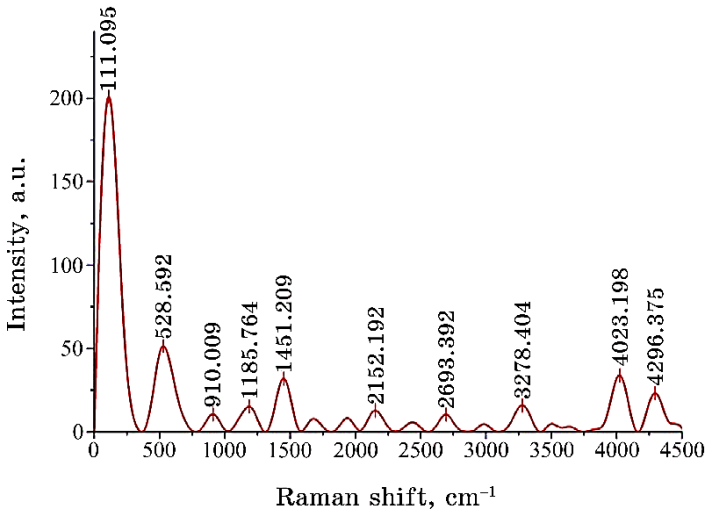

Fig. 7. Raman spectrum of photoanode.

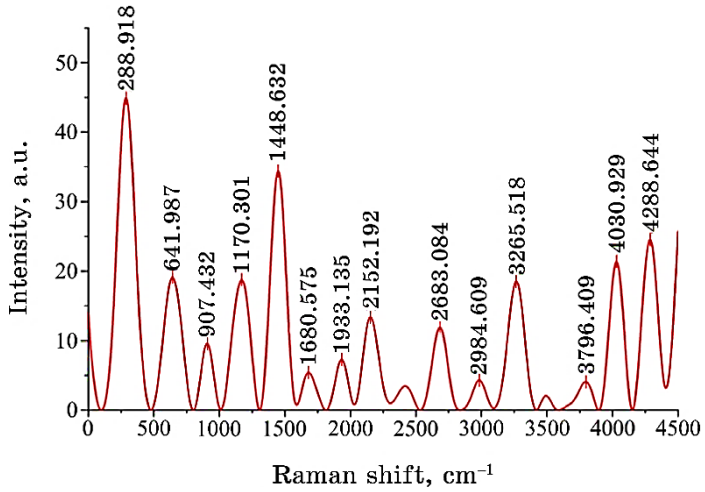

Fig. 8. Raman spectrum of Cathode 1.

additional peaks at 1185 cm^{-1} attributed to poorly structured graphite or the *D*-band [25]. The Raman spectrum of TiO_2 is well-known, with the rutile tetragonal phase containing four Raman active modes ($A_{1g} + B_{1g} + B_{2g} + E_g$) and the anatase phase having six Raman active modes ($A_{1g} + 2B_{1g} + 3E_g$) [23].

Figure 9 demonstrates two distinct anatase phase peaks at 111 (B_{1g}) and 592 (B_{1g}) E_g in TiO_2 nanoparticle samples, with no rutile phase Raman peaks observed. Vibrational modes in nanoparticle

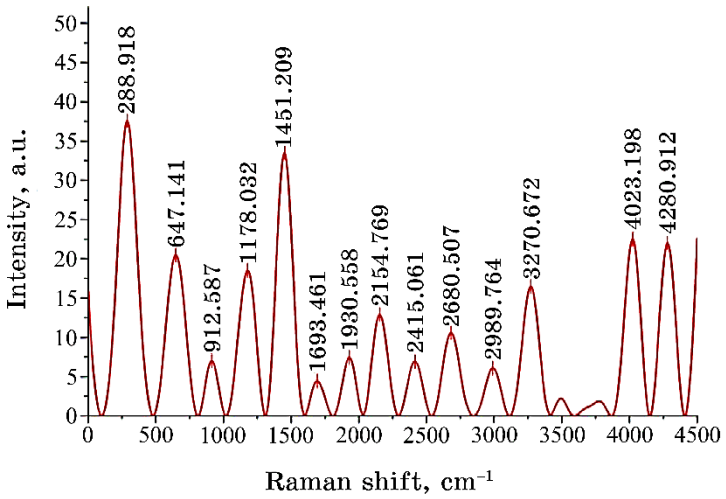

Fig. 9. Raman spectrum of Cathode 2.

composites coated with Ag nanoparticles are influenced by the connections between components resulting from chemical or physical interactions. The phonon confinement effect may explain the wavenumber shift and/or widening of Raman peaks observed [26, 27]. Due to the high refraction index of TiO_2, the surface band of Ag–TiO_2 supported on CNT nanoparticles is red-shifted and widened. The *D*-band and *G*-band of $AgTiO_2$–CNT nanoparticle composites display blue shifts, which can be attributed to adhesion between Ag–TiO_2 nanoparticles and CNTs, as well as strain effects at the Ag–TiO_2–CNT interface [28].

The Raman spectra indicate significant dissimilarities in the chemical arrangement of PPy_SDS. Enhanced charge carrier proportion in PPy_SDS is manifested by intensified bands, which are typically linked to the dictation species at 288, 1448, 4030, and 3256 cm^{-1} [29]. Additionally, the extent of conjugation in PPy can be estimated by the intensity ratio of vibrations within the 1680–2948 cm^{-1} range. Based on this, the conjugation length in the PPy_SDS film is considerably extensive [30].

The Raman spectra of the PPy/SDS–MWCNT electrode were examined using a wavelength of 514 nm. A significant modification near 1000–1500 cm^{-1} was observed, indicating that functional groups were attached to the surface [31]. In the Raman spectra of the PPy–MWCNT composite films, the characteristic peak of pure MWCNT at 1693 cm^{-1} is associated with the E_{2g} mode of the graphite wall [32]. It has been theoretically predicted that a single-cylinder nanotube would exhibit an E_{2g} mode at 1930 cm^{-1} [33]. The Raman spectra of the composite films displayed bands correspond-

ing to both pure PPy and MWCNT. Additionally, the intensity of the band located at 1451 cm^{-1} escalated with the increase of the MWCNT to pyrrole feeding mass ratio, indicating an increase in MWCNT content within the composite film [34].

3.4. Atomic Force Microscopy (AFM)

3.4.1. Atomic Force Microscopy (AFM) of Photoanode

TiO_2 nanoparticles influence surface roughness and height metrics including root mean square height (R_q) and total height (R_t). TiO_2 nanoparticles may provide a somewhat rough surface with large height variations. TiO_2 nanoparticles can also have an impact on spatial characteristics like autocorrelation length (R_{al}) and dominant spatial wavelength (R_{sw}). TiO_2 nanoparticle size and distribution may introduce periodic patterns and influence the overall surface structure. The TiO_2 coating could have an effect on the material ratio characteristics (R_{mr} and R_{mc}).

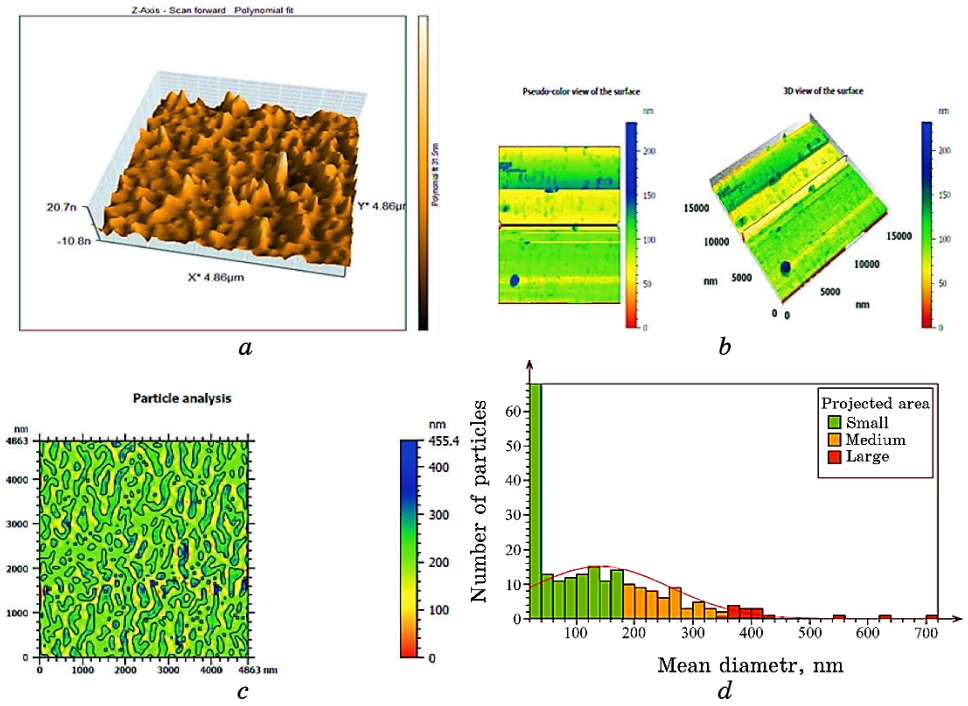

Fig. 10. AFM images of photoanode: (*a*) surface topography; (*b*) 3*D* view of the surface; (*c*) particle analysis; (*d*) histogram.

TABLE 2. AFM parameters of photoanode.

Height parameter				
R_q	13.67	nm		Root mean square height
R_{sk}	2.861			Skewness
R_{ku}	11.45			Kurtosis
R_t	75.99	nm		Total height
R_{pt}	59.19	nm	Max of values on: All λ_c (1)	Maximum hill height
R_p	59.19	nm	Average of values on: All λ_c (1)	Mean hill height
R_{vt}	16.80	nm	Max of values on: All λ_c (1)	Maximum dale depth
R_v	16.80	nm	Average of values on: All λ_c (1)	Mean dale depth
R_{zx}	75.99	nm	Max of values on: All λ_c (1)	Maximum height
R_z	75.99	nm	Average of values on: All λ_c (1)	Mean height
R_a	8.312	nm		Arithmetic mean absolute height
Spatial parameters				
R_{al}	492.6	nm	$s = 0.2$	Autocorrelation length
R_{sw}	3012	nm		Dominant spatial wavelength
Hybrid parameters				
R_{dq}	3.850			Root mean square gradient
R_{da}	1.968			Arithmetic mean absolute gradient
R_{dt}	23.30			Maximum absolute gradient
R_{dl}	14031	nm		Developed length
R_{dr}	0.2231	%		Developed length ratio
Material ratio parameters				
R_{mr}	100.0	%	c = 1000 nm below highest peak	Material ratio
R_{mc}	55.09	nm	$p = 20\%$	Inverse material ratio
R_{dc}	12.53	nm	$p = 20\%$, $q = 80\%$	Profile section height difference
Feature parameters (element)				
R_{sm}	1410	nm		Mean width of the profile elements
R_{smx}	3174	nm		Maximum profile element width
R_{smq}	845.9	nm		Standard deviation of profile element width
R_c	21.00	nm		Mean height of the profile elements
R_{cx}	68.67	nm		Maximum height profile elements

A uniform and evenly distributed TiO_2 layer would result in a

greater material ratio and more even TiO_2 distribution across the surface [35].

On the other hand, MWCNTs may affect the height parameters (R_q, R_t) by introducing extra surface characteristics such as nanotube bundles or agglomerates. These characteristics may lead to overall roughness and height differences.

MWCNTs can also have an effect on hybrid parameters like root mean square gradient (R_{dq}) and maximum absolute gradient (R_{dt}). The presence of MWCNTs with their distinctive cylindrical architecture may cause variations in surface slope and greater gradient values.

By introducing elongated and tubular structures to the surface, MWCNTs may alter the feature parameters (R_{sm}, R_{smx}, R_{smq}), resulting in wider and more diversified feature sizes [36].

Furthermore, Ag nanoparticles on the surface may contribute to the height parameters (R_q, R_t) by producing localized agglomerations or clusters. These agglomerations can cause height fluctuations and enhance roughness overall.

By incorporating Ag nanoparticles, the material ratio characteristics (R_{mr}, R_{mc}) may be influenced by introducing areas with increased Ag concentration. This can cause localized differences in material distribution and have an impact on the overall material ratio.

By introducing extra nanoscale features or clusters, Ag nanoparticles can also alter the feature parameters (R_{sm}, R_{smx}, R_{smq}). These characteristics can contribute to larger feature sizes and greater feature width variability [37].

3.4.2. Atomic Force Microscopy (AFM) of Cathode 1

The aforementioned AFM results can be related to polypyrrole ability to generate a rough and porous structure, which can lead to an enhanced roughness parameter such as R_q [34]. Polypyrrole rough surface shape provides for a higher surface area, which promotes dye adsorption and facilitates charge transfer inside the cathode [38].

Sodium dodecyl sulphate (SDS), on the other hand, is a surfactant that is frequently used to change the surface characteristics of materials. The addition of SDS surfactant to the DSSC cathode can impact surface shape and improve film formation [39].

Surfactant molecules can improve wetting qualities and assist the creation of a smoother, more uniform layer. This might result in reduced surface roughness (lower R_q) and smoother surface characteristics, as shown by smaller changes in height metrics like R_{pt} and R_p [40].

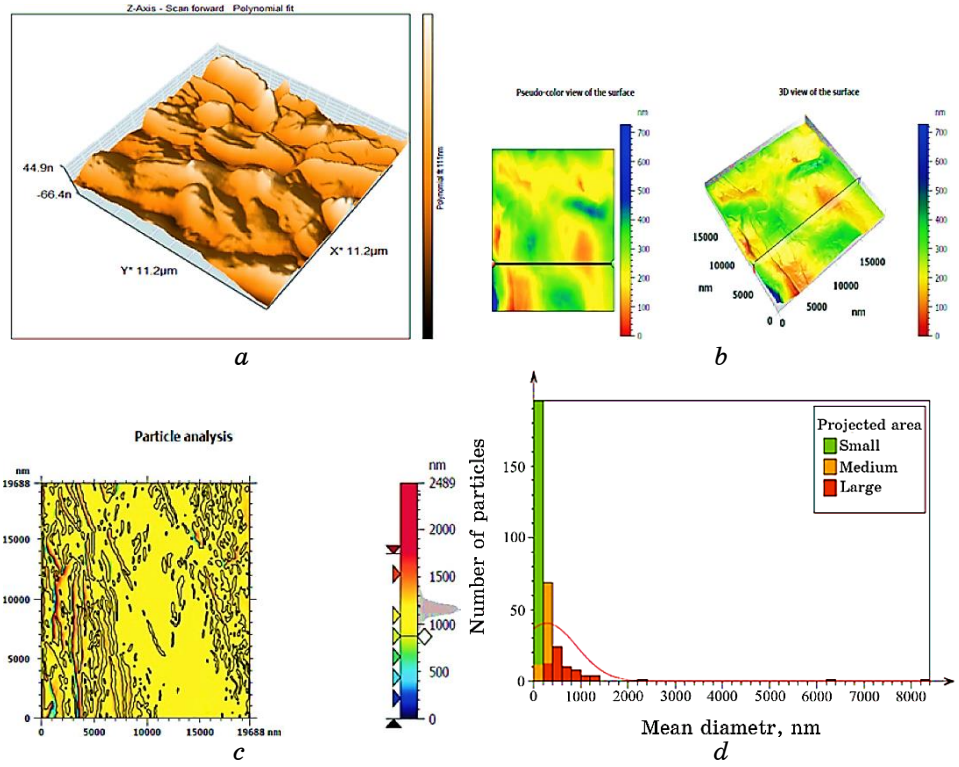

Fig. 11. AFM images of Cathode 1: (*a*) surface topography; (*b*) 3*D* view of the surface; (*c*) particle analysis; (*d*) histogram.

3.4.3. Atomic Force Microscopy (AFM) of Cathode 2

The root mean square height (R_q) and total height (R_t) measures show that PPy contributes to the overall roughness of the cathode surface. Because of its naturally textured and irregular structure, the presence of PPy promotes surface roughness.

The spatial parameters autocorrelation length (R_{al}) and dominant spatial wavelength (R_{sw}) are likewise influenced by PPy. These metrics show the presence of periodic structures or recurring patterns that can be caused by the arrangement and alignment of PPy chains inside the cathode [41].

The material ratio parameter (R_{mr}) indicates that PPy distributes uniformly throughout the surface features. It means that PPy helps to generate the surface roughness, elevations, and depressions seen in the AFM studies.

The profile section height difference (R_{dc}) parameter, which reflects the height difference between preset portions of the surface

profile, may also be affected by PPy.

TABLE 3. AFM parameters of Cathode 1.

Height parameter				
R_q	51.46	nm		Root mean square height
R_{sk}	0.001505			Skewness
R_{ku}	2.018			Kurtosis
R_t	213.7	nm		Total height
R_{pt}	116.9	nm	Max of values on: All λ_c (1)	Maximum hill height
R_p	116.9	nm	Average of values on: All λ_c (1)	Mean hill height
R_{vt}	89.70	nm	Max of values on: All λ_c (1)	Maximum dale depth
R_v	89.70	nm	Average of values on: All λ_c (1)	Mean dale depth
R_{zx}	206.6	nm	Max of values on: All λ_c (1)	Maximum height
R_z	206.6	nm	Average of values on: All λ_c (1)	Mean height
R_a	44.00	nm		Arithmetic mean absolute height
Spatial parameters				
R_{al}	1736	nm	$s = 0.2$	Autocorrelation length
R_{sw}	9882	nm		Dominant spatial wavelength
Hybrid parameters				
R_{dq}	3.359			Root mean square gradient
R_{da}	2.381			Arithmetic mean absolute gradient
R_{dt}	13.55			Maximum absolute gradient
R_{dl}	19025	nm		Developed length
R_{dr}	0.1721	%		Developed length ratio
Material ratio parameters				
R_{mr}	100.0	%	$c = 1000$ nm below highest peak	Material ratio
R_{mc}	77.86	nm	$p = 20\%$	Inverse material ratio
R_{dc}	100.4	nm	$p = 20\%$, $q = 80\%$	Profile section height difference
Feature parameters (element)				
R_{sm}	11506	nm		Mean width of the profile elements
R_{smx}	11891	nm		Maximum profile element width
R_{smq}	11519	nm		Standard deviation of profile element width
R_c	145.7	nm		Mean height of the profile elements
R_{cx}	152.6	nm		Maximum height profile elements

Because of its organization and distribution inside the cathode, PPy presence may cause changes in height across various portions [42].

Moreover MWCNTs contribute significantly to the roughness and texture of the cathode surface. They contribute to the parameters of root mean square height (R_q), total height (R_t), and maximum height (R_{zx}), resulting in a rough surface morphology.

MWCNTs have an effect on slope variations, as evidenced by the root mean square gradient (R_{dq}) and arithmetic mean absolute gradient (R_{da}) parameters. MWCNTs create linked networks or clusters on the surface, introducing different slope angles.

MWCNTs can also have an effect on the developed length (R_{dl}) parameter, which measures the length of the surface features that have been produced. MWCNTs can cause prolonged features or structures that contribute to the total developed length [43].

The material ratio parameter (R_{mr}) demonstrates that MWCNTs are uniformly distributed across the surface characteristics, emphasizing their contribution to the roughness and elevations reported

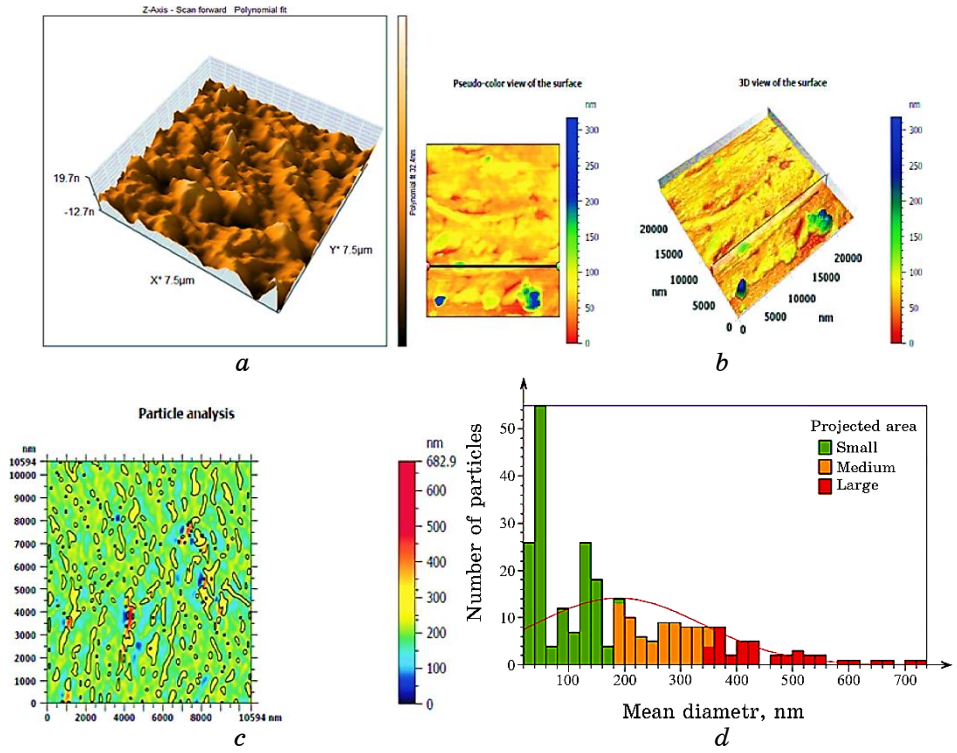

Fig. 12. AFM images of Cathode 2: (*a*) surface topography; (*b*) 3*D* view of the surface; (*c*) particle analysis; (*d*) histogram.

in the AFM data.

TABLE 4. AFM parameters of Cathode 2.

Height parameter				
R_q	24.55	nm		Root mean square height
R_{sk}	1.028			Skewness
R_{ku}	3.861			Kurtosis
R_t	104.1	nm		Total height
R_{pt}	67.26	nm	Max of values on: All λ_c (1)	Maximum hill height
R_p	67.26	nm	Average of values on: All λ_c (1)	Mean hill height
R_{vt}	36.88	nm	Max of values on: All λ_c (1)	Maximum dale depth
R_v	36.88	nm	Average of values on: All λ_c (1)	Mean dale depth
R_{zx}	104.1	nm	Max of values on: All λ_c (1)	Maximum height
R_z	104.1	nm	Average of values on: All λ_c (1)	Mean height
R_a	18.76	nm		Arithmetic mean absolute height
Spatial parameters				
R_{al}	1386	nm	$s = 0.2$	Autocorrelation length
R_{sw}	12047	nm		Dominant spatial wavelength
Hybrid parameters				
R_{dq}	1.826			Root mean square gradient
R_{da}	1.153			Arithmetic mean absolute gradient
R_{dt}	8.645			Maximum absolute gradient
R_{dl}	19021	nm		Developed length
R_{dr}	0.05095	%		Developed length ratio
Material ratio parameters				
R_{mr}	100.0	%	$c = 1000$ nm below highest peak	Material ratio
R_{mc}	56.73	nm	$p = 20\%$	Inverse material ratio
R_{dc}	31.45	nm	$p = 20\%$, $q = 80\%$	Profile section height difference
Feature parameters (element)				
R_{sm}	7555	nm		Mean width of the profile elements
R_{smx}	7555	nm		Maximum profile element width
R_{smq}	*****	nm		Standard deviation of profile element width
R_c	93.60	nm		Mean height of the profile elements
R_{cx}	93.60	nm		Maximum height profile elements

The metrics mean width of profile elements (R_{sm}) and maximum width of profile elements (R_{smx}) show the existence of broad surface features, which can be linked to the presence of MWCNTs [44].

SDS surfactant is often used to improve the dispersion and stability of carbon nanotubes in solution, such as MWCNTs. It aids in the uniform dispersion of MWCNTs and inhibits agglomeration during the production process. The presence of SDS surfactant may have an indirect effect on surface roughness and texture by influencing the dispersion and arrangement of MWCNTs within the cathode [45]. From AFM results, it is clearly observed that C_1 has a higher roughness (R_q) and total height (R_t) than C_2, indicating a rougher surface with larger height variability. MWCNTs in C_1 may aid in the creation of higher structures and deeper troughs, resulting in greater surface roughness. Also, C_2 has a lower autocorrelation length (R_{al}) than C_1, indicating a distinct periodicity or spatial arrangement of surface features. Furthermore, the dominating spatial wavelength (R_{sw}) in C_2 is much higher, indicating the presence of unique and larger-scale surface patterns.

The surface properties of cathodes revealed by AFM can have an impact on their performance. A rougher surface (as seen in C_1) may provide more active areas for catalytic processes while also increasing light absorption. Excessive roughness, on the other hand, can result in higher charge recombination and decreased efficiency. The smoother surface of C_2, on the other hand, may offer superior charge transport capabilities and lower surface-related losses.

3.5. The Photovoltaic Performance of Prepared DSSCs

The anode material (PHOTOANODE), namely, TiO_2–MWCNT–Ag nanoparticles, plays a crucial role in enhancing the efficiency of DSSCs. TiO_2 component acts as the main electron acceptor and provides a large surface area for dye adsorption provides a high surface area for dye adsorption and plasmonic effects. The presence of MWCNTs improves electron transport, while the incorporation of Ag nanoparticles and these factors contribute to efficient charge generation, transport, and collection, resulting in higher overall device efficiency. However, the specific impact of the anode material may vary depending on the choice of dye and cathode materials used in the configuration [46]. The efficiency of DSSCs can be influenced by various factors, including the choice of dye, cathode material, and the resulting interactions between the dye, photoanode, and cathode. The use of Z907 dye generally leads to higher efficiencies compared to plant extracts. However, the choice of cathode material can also play a significant role in enhancing the performance of DSSCs, as demonstrated by the improved efficien-

cies observed in configurations using C_2 except in the case of PHOTOANODE + C_1 + Z907 DSSCs which me be attributed to synergistic Interaction where the combination of C_1 (polypyrrole and SDS surfactant) with Z907 dye may result in a more favourable and efficient interaction between the dye molecules and the photoanode (PHOTOANODE). This synergistic interaction can enhance the light absorption, charge separation, and transport processes within the DSSC, leading to improved performance and higher efficiency [47]. Moreover, the energy levels of the components in C_1, including the poly pyrrole and SDS surfactant, may be better aligned with the energy levels of Z907 dye and the photoanode material (TiO_2–MWCNT–Ag). This alignment can facilitate efficient electron injection from the excited dye molecules into the conduction band of the photoanode, minimizing energy losses and improving overall device performance [48]. Also, composition of C_1 may provide better charge transport properties, allowing for efficient extraction and collection of photo-generated electrons from the photoanode. This improved charge transport can minimize electron recombination and ensure a high current output, resulting in higher short-circuit current (I_{sc}) and overall efficiency [49]. Eventually, the characteristics of C_1 may promote better dye adsorption and coverage on the photoanode surface, ensuring a higher dye loading and maximizing light harvesting. This optimized dye adsorption can enhance the utilization of incident photons and increase the photocurrent, contributing to higher efficiency.

In contrast, while C_2 (polypyrrole, SDS, and MWCNT) may provide certain advantages for specific dyes (Hab., Pom., Aru.) in terms of charge transport or energy level alignment, it may not be as suitable for the Z907 dye. The specific interaction between C_2 and Z907 may be less favourable, resulting in lower efficiency compared to the C_1 configuration [50].

TABLE 5. Photovoltaic properties of DSSCs with different counter electrodes and different dyes.

Compounds	V_{oc}	I_{sc}	V_{max}	I_{max}	*FF*	η, %
$A_1 + C_1$ + Z907	0.807	15.1	0.72	14.1	0.833	2.537
$A_1 + C_1$ + Hab.	0.52	9.8	0.49	9	0.865	1.102
$A_1 + C_1$ + Pom.	0.252	17.6	0.24	17.5	0.946	1.04
$A_1 + C_1$ + Aru.	0.326	7.6	0.3	6.5	0.86	0.535
$A_1 + C_2$ + Z907	0.496	24.5	0.45	21.8	0.807	2.453
$A_1 + C_2$ + Aru.	0.749	8.8	0.67	8.6	0.874	1.44
$A_1 + C_2$ + Hab.	0.435	12.9	0.43	11.5	0.898	1.24
$A_1 + C_2$ + Pom.	0.463	13.9	0.39	12.5	0.946	1.16

3.6. The Work Principle of DSSCs

The working principle of DSSC can be explained with the help of Figs. 13–15.

Photosensitize absorbs electrons when light is incident on it:

$$Z_{907} + h\nu \rightarrow Z_{907}^{*} . \quad (1)$$

After that, the excitation sensitizer Z907* introduces an electron into the semiconductor conduction band:

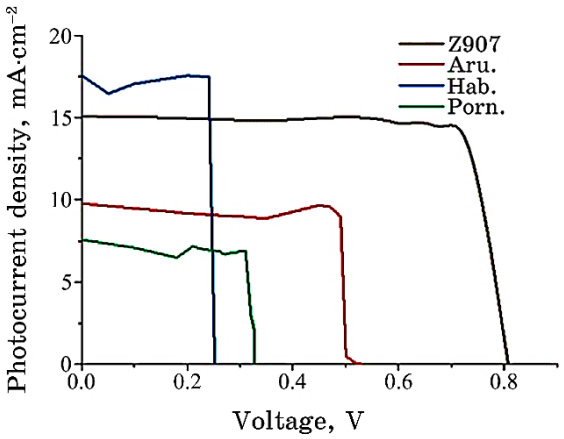

Fig. 13. Current density–voltage (I–V) curves for DSSCs for counter electrode C_1 employing different dyes.

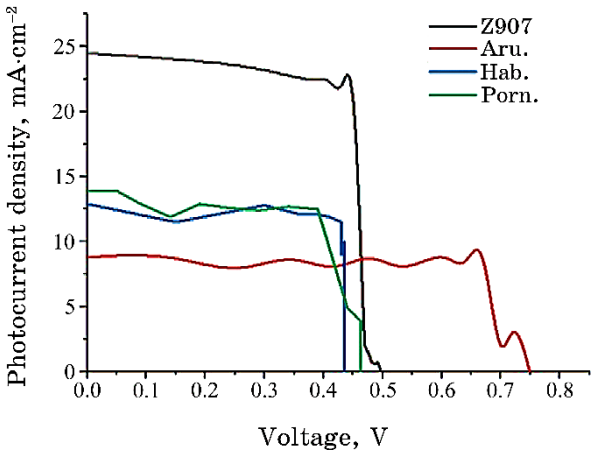

Fig. 14. Current density–voltage (I–V) curves for DSSCs for counter electrode C_2 employing different dyes.

$$Z^*_{907} \rightarrow Z^+_{907} + e^-_{(\text{injected})} \ . \quad (2)$$

Now, these electrons are transferred into the upper bands, called the conduction band of TiO_2. The liquid electrolyte I^- / I^{3-} couple helps the electrons to return to the dye through external load:

$$I^-_3 + 2e^-_{(\text{counter electrode})} \rightarrow 3I^- , \quad (3)$$

$$Z^+_{907} + \frac{3}{2} I^- \rightarrow Z_{907} + \frac{1}{2} I^-_3 , \quad (4)$$

$$Z^+_{907} + e^-_{TiO_2} \rightarrow Z_{907} , \quad (5)$$

$$2e^-_{TiO_2} + I^-_3 \rightarrow 3I^-_{(TiO_2/Ag/MWCNT)} . \quad (6)$$

This movement of electrons creates a current [51].

In general, the composition of the photocathodes can have a significant impact on their performance and efficiency, Cathode 1 Composition: polypyrrole, SDS surfactant, and MWCNT [52].

Polypyrrole (PPy) is a polymer with strong electrical conductivity and electrocatalytic characteristics. It can improve charge transfer efficiency and provide a pathway for electron transport in the photocathode [53].

SDS (sodium dodecyl sulphate) is a surfactant that is often used to improve the dispersion and stability of nanoparticles. SDS might help in the dispersion of MWCNT (Multi-Walled Carbon Nanotubes) within the polypyrrole matrix in the context of PC1 [54].

MWCNTs are multilayered carbon nanotubes. They have high electrical conductivity and can improve the photocathode's charge transport capabilities. MWCNTs can also provide more surface area for catalytic processes, potentially increasing the efficiency of the photocathode [55].

C_2 is a simpler structure than C_1 since it lacks the incorporation

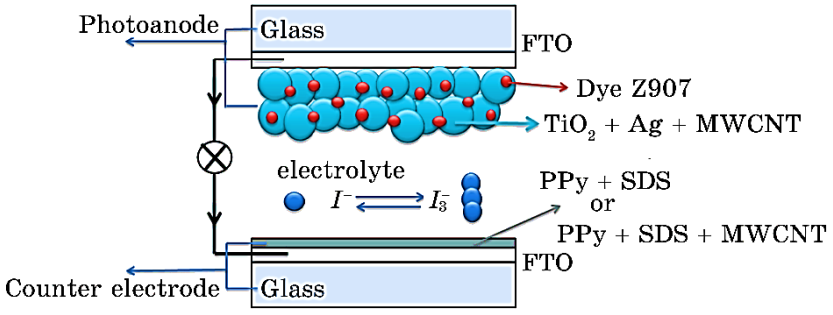

Fig. 15. Dye-sensitized solar-cells' scheme.

of MWCNTs in its composition. Polypyrrole (PPy) continues to be the most important conducting polymer in C_2, contributing to charge transfer and electron transport mechanisms. SDS surfactant is once again present in C_2 to aid in polypyrrole dispersion and stability [56].

Because carbon nanotubes have good conductive qualities, the insertion of MWCNTs in C_1 may improve the total conductivity of the photocathode. This increased conductivity may allow for more effective charge transport and extraction, perhaps leading to higher efficiency than C_2 [57].

The presence of MWCNTs in C_1 may provide additional catalytic sites for electrochemical processes, thus, boosting the catalytic activity, and performance of the photocathode also may influence surface morphology, potentially resulting in a rougher surface with a larger surface area. This expanded surface area can improve light absorption and charge generation efficiency. MWCNTs in C_1 may affect photocathode stability due to interactions between the carbon nanotubes and the surrounding components. However, the particular implications on stability would be dependent on the fabrication method and component compatibility [58].

3.7. The Effect of Dyes

The choice of dyes in dye-sensitized solar cells (DSSCs) plays a crucial role in determining the efficiency of the solar cell. Different dyes exhibit variations in light absorption properties, energy levels, and electron injection efficiencies, which directly impact the overall performance of the DSSCs [59].

This can be explained accordingly. Z907 is a specific dye used in DSSCs. The impact of Z907 on DSSC efficiency is as follows.

a. Light Absorption: Z907 dye has a broad absorption spectrum, allowing it to capture a wide range of sunlight wavelengths. This broad absorption capability increases the overall light harvesting efficiency of the solar cell, enhancing its performance.

b. Energy Level Alignment: The energy levels of the Z907 dye are optimized to facilitate efficient electron injection from the excited dye molecule to the semiconductor electrode (*e.g.*, TiO_2). This efficient electron injection minimizes charge recombination and enhances the overall efficiency of the solar cell [60].

1. Pomegranate Juice: Pomegranate juice contains natural pigments, such as anthocyanins, which can serve as sensitizers in DSSCs. The impact of pomegranate juice as a dye in DSSCs can be as follows.

a. Light Absorption: Pomegranate juice contains anthocyanins that can absorb a broad range of visible light wavelengths. This

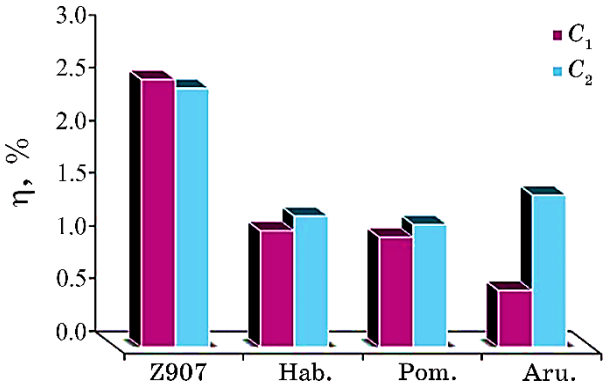

Fig. 16. Scheme for evaluating the efficiency of dyes on PHOTOANODE.

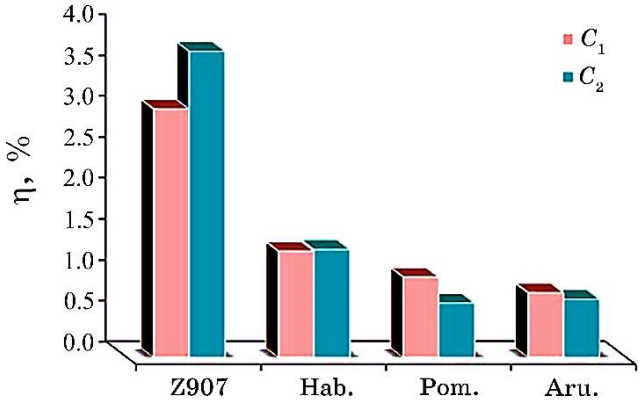

Fig. 17. Scheme for evaluating the efficiency of dyes on PA2.

broad absorption spectrum allows for efficient harvesting of solar radiation, leading to improved light absorption and higher efficiency of DSSCs.

b. Charge Injection Efficiency: Anthocyanins in pomegranate juice can effectively inject electrons into the conduction band of the semiconductor (*e.g.*, TiO_2). This efficient charge injection minimizes charge recombination, thus enhancing the overall performance and efficiency of the DSSC.

c. Stability: The stability of pomegranate juice-based dyes in DSSCs is a crucial factor. Anthocyanins can be susceptible to degradation under prolonged exposure to light and environmental conditions. Therefore, strategies to enhance the stability of pomegranate juice dyes, such as encapsulation or chemical modification, may be necessary to improve the long-term performance of DSSCs [61].

2. Spinach Leaf Extract: Spinach leaf extract contains chloro-

phyll pigments that can be utilized as sensitizers in DSSCs. The impact of spinach leaf extract as a dye in DSSCs can be as follows:

a. Light Absorption: Chlorophyll pigments in spinach leaves have strong absorption in the blue and red regions of the visible spectrum. This absorption profile allows for efficient light harvesting and enhances the overall light absorption capability of DSSCs.

b. Electron Injection Efficiency: Chlorophyll pigments possess suitable energy levels for efficient electron injection into the conduction band of the semiconductor. This efficient electron injection process reduces charge recombination, leading to improved device performance and higher DSSC efficiency.

c. Sensitizer Loading and Stability: Optimizing the loading concentration of spinach leaf extract in DSSCs is crucial to achieve an appropriate balance between light absorption and charge injection. Additionally, the stability of chlorophyll-based dyes under light exposure and environmental factors should be considered to ensure long-term device performance [62].

3. Hibiscus (Roselle) Flower Extract: Hibiscus (Roselle) flower extract contains various pigments, including anthocyanins, which can be used as sensitizers in DSSCs. The impact of hibiscus flower extract as a dye in DSSCs can be as follows:

a. Light Absorption: Anthocyanin pigments present in hibiscus flowers exhibit strong absorption in the visible light region, particularly in the blue and red wavelengths. This characteristic enables efficient light harvesting, contributing to enhanced light absorption and improved DSSC efficiency.

b. Electron Injection Efficiency: Hibiscus flower extract dyes can facilitate efficient electron injection into the semiconductor, promoting efficient charge separation and reducing recombination. This attribute positively influences the overall performance and efficiency of the DSSC.

c. pH Sensitivity: Anthocyanin pigments in hibiscus flower extract can exhibit pH-dependent properties. It is important to consider the pH conditions during the extraction process and optimize the pH of the electrolyte to maintain stable dye performance and maximize the efficiency of the DSSCs [63].

4. CONCLUSION

In conclusion, the anode material, cathode composition, and dye selection all have an impact on the efficiency of dye-sensitized solar cells (DSSCs). The anode material (TiO_2–MWCNT–Ag nanoparticles) improves efficiency by increasing dye adsorption surface area and boosting electron transport. The dye used, such as Z907, is critical in achieving effective light absorption and energy level alignment

for electron injection. Because of increased charge transfer, extraction of photo-generated electrons, and optimal dye adsorption, the cathode composition C_1 (polypyrrole, SDS surfactant, and MWCNT) performs better with Z907 dye. Other colours, including as pomegranate juice, spinach leaf extract, and hibiscus flower extract, have an effect on DSSC efficiency due to their light absorption and electron injection efficiencies. Understanding these interactions is critical for developing high-efficiency DSSCs and moving renewable energy technologies forward.

ACKNOWLEDGEMENTS

The authors offer their appreciations for Al-Qadisiyah University, College of science Chemistry Department for its instrumental and technical support.

REFERENCES

1. B. O'regan and M. Grätzel, *Nature*, **353**, Iss. 6346: 737 (1991); doi:10.1038/353737a0
2. N. Gokilamani, N. Muthukumarasamy, M. Thambidurai, A. Ranjitha, and D. Velauthapillai, *J. Sol–Gel Sci. Technol.*, **66**, Iss. 2: 212 (2013); doi:10.1007/s10971-013-2994-9
3. N. Memarian, I. Concina, A. Braga, S. M. Rozati, A. Vomiero, and G. Sberveglieri, *Angewandte Chemie*, **123**, Iss. 51: 12529 (2011); https://doi.org/10.1002/ange.201104605
4. R. Bart, P. Sandeep, and S. Ullrich, *Chemical Society Reviews*, **44**, Iss. 22: 8326 (2015); https://doi.org/10.1039/C5CS00352K
5. H. J. Hwang and H. S. Kim, *Journal of Composite Materials*, **48**, Iss. 14: 1679 (2014); doi:10.1177/0021998313490215
6. C. Hyonkwang, K. Hyunkook, H. Sookhyun, H. Youngmoon, and J. Minhyon, *J. Mater. Chem.*, **21**, Iss. 21: 7548 (2011); https://doi.org/10.1039/C1JM11145K
7. G. Feng, W. Hong, X. Xin, Z. Gang, and W. Zhong-Sheng, *J. Am. Chem. Soc.*, **134**, Iss. 26: 10953 (2012); doi:10.1021/ja303034w
8. J. Wu, Q. Li, L. Fan, Z. Lan, P. Li, J. Lin, and S. Hao, *J. Power Sources*, **181**, Iss. 1: 172 (2008); https://doi.org/10.1016/j.jpowsour.2008.03.029
9. T. C. T. Thanh, P. J. Young, L. S. Woo, S. Thogiti, and K. J. Hong, *J. Nanosci. Nanotechnol.*, **16**, Iss. 5: 5263 (2016); https://doi.org/10.1166/jnn.2016.12266
10. K. B. Erande, P. Y. Hawaldar, S. R. Suryawanshi, B. M. Babar, A. A. Mohite, H. D. Shelke, S. V. Nipane, and U. T. Pawar, *Materials Today*, **43**, Iss. 4: 2716 (2021); https://doi.org/10.1016/j.matpr.2020.06.357
11. R. F. Mansa, G. Govindasamy, Y. Y. Farm, H. Abu Bakar, J. Dayou, and C. S. Sipaut, *Journal of Physical Science*, **25**, Iss. 2: 85 (2014);
12. S. A. Taya, T. M. El-Agez, H. S. El-Ghamri, and M. S. Abdel-Latif, *International Journal of Materials Science and Applications*, **2**, Iss. 2: 37 (2013);

doi:10.11648/j.ijmsa.20130202.11
13. L. Chun Hung, S. Ryan, and C. B. O'Regan, *Journal of Materials Chemistry A*, **1**, Iss. 45: 14154 (2013); https://doi.org/10.1039/C3TA13145A
14. Md. H. Miah and S. Miah, *Asian Journal of Applied Sciences*, **3**, Iss. 4: 806 (2015).
15. Sung Ho Song, Ho-Kyun Jeong, Yong-Gu Kang, and Choon-Tack Cho, *Polymer (Korea)*, **34**, Iss. 2: 108 (2010); doi:10.7317/pk.2010.34.2.108
16. K. R. Gota and S. Suresh, *Asian Journal of Chemistry*, **26**, Iss. 21: 7087 (2014); doi:10.14233/ajchem.2014.17142
17. R. S. Dubey, K. V. Krishnamurthy, and S. Singh, *Results in Physics*, **14**: 102390 (2019); https://doi.org/10.1016/j.rinp.2019.102390
18. B. Ajitha, Y. A. K. Reddy, and R. P. Sreedhara, *Molecular and Biomolecular Spectroscopy*, **121**: 164 (2014); doi:10.1016/j.saa.2013.10.077
19. Y. D. Guang, Z. B. Y. W. Li, and Qian, *International Journal of Nanomedicine*, **6**: 3271 (2011); https://doi.org/10.2147/IJN.S27468
20. H. Vijeth, K. S. P. Ashok, L. Yesappa, M. Niranjana, M. Vandana, and H. Devendrappa, *AIP Conference Proceedings*, **2142**, Iss. 1: 150029 (2019); https://doi.org/10.1063/1.5122578
21. M. A. Rashed, M. Faisal, M. Alsaiari, S. A. Alsareii, and F. A. Harraz, *Electrocatalysis*, **12**: 650 (2021); https://doi.org/10.1007/s12678-021-00675-6
22. R. M. Mohammad, S. A. Duha, and A. K. M. Mustafa, *Journal of Sol–Gel Science and Technology*, **90**: 498 (2019); doi:10.1007/s10971-019-04973-w
23. H. Rhee et al., *Synthetic Metals*, **28**, Iss. 1–2: 605 (1989).
24. S. Hiroshi, O. Kentaro, K. Daisuke, D. Bhavana, S. Usha, and N. Tsutomu, *Journal of the Electrochemical Society*, **150**, Iss. 5: H119 (2003); doi:10.1149/1.1566420
25. Yang Zhao, Yue Hu, Yan Li, Han Zhang, Shaowen Zhang, Liangti Qu, Gaoquan Shi, and Liming Dai, *Nanotechnology*, **21**, Iss. 50: 505702 (2010); doi:10.1088/0957-4484/21/50/505702
26. P. P. Lottici, D. Bersani, M. Braghini and A. Montenero, *Journal of Materials Science*, **28**, Iss. 1: 177 (1993); doi:10.1007/bf00349049
27. N. K. Konstantin, O. Bulent, C. S. Hannes, K. P. Robert, A. A. Ilhan, and C. Roberto, *Nano Letters*, **8**, Iss. 1: 36 (2008); https://doi.org/10.1021/nl071822y
28. H. Chang, H.T. Jung, C. Tien-Li, H. K. David, J.C. Song and C. S. Hua, *Materials Transactions*, **50**, Iss. 12: 2879 (2009); https://doi.org/10.2320/matertrans.M2009203
29. Y. Furukawa, S. Tazawa, Y. Fujii, and I. Harada, *Synthetic Metals*, **24**, Iss. 4: 329 (1988); https://doi.org/10.1016/0379-6779(88)90309-8
30. D. C. Sophie and S. P. Yves, *Chemistry of Materials*, **11**, Iss. 3: 829 (1999); https://doi.org/10.1021/cm9807541
31. C. D. Chouvy and T. T. M. Tran, *Electrochemistry Communications*, **10**, Iss. 6: 947 (2008); https://doi.org/10.1016/j.elecom.2008.04.024
32. H. Hiura, T. W. Ebbesen, K. Tanigaki, and H. Takahashi, *Chemical Physics Letters*, **202**, Iss. 6: 509 (1993); https://doi.org/10.1016/0009-2614(93)90040-8
33. R. A. Jishi, L. Venkataraman, M. S. Dresselhaus, and G. Dresselhaus, *Chemical Physics Letters*, **209**, Iss. 1–2: 77 (1993); https://doi.org/10.1016/0009-

2614(93)87205-H
34. M. F. Islam, E. Rojas, D. M. Bergey, A. T. Johnson, and A. G. Yodh, *Nano Letters*, **3**, Iss. 2: 269 (2003); https://doi.org/10.1021/nl025924u
35. W. C. Oh and M. L. Chen, *Chemical Society*, **29**, Iss. 1: 159 (2008); doi:10.5012/bkcs.2008.29.1.159
36. K. Youngmi, L. Ginaya; C. Boyce, Y. Yeoheung, N. S. Vesselin, S. Mark, P. Devdas, and S. Jagannathan, *Composites Part B: Engineering*, **57**: 105 (2014); https://doi.org/10.1016/j.compositesb.2013.09.004
37. C. Ling-Yu, L. Chun-Ting, L. Yu-Yan, L. Chuan-Pei, Y. Min-Hsin, H. Kuo-Chuan, and L. Jiang-Jen, *Electrochimica Acta*, **155**: 263 (2015); https://doi.org/10.1016/j.electacta.2014.12.127
38. S. V. Ahmad, M. M. Ghasem, and J. Majid, *Synthetic Metals*, **191**: 104 (2014); https://doi.org/10.1016/j.synthmet.2014.02.021
39. L. Woranan, K. T. Chyuan, S. Chaochin, S. Pedaballi, K. Sasipriya, L. Ya-Fen, C. Bo-Ren, and L. Wen-Ren, *Solar Energy*, **142**: 1 (2017); https://doi.org/10.1016/j.solener.2016.12.017
40. I. M. V. Ana, G. G. Emilio, J. A. María, and J. G. S. María, *Solar Energy*, **91**: 263 (2013); https://doi.org/10.1016/j.solener.2013.02.009
41. C. Sadik, E. E. Sule, Ali, A. A. Khalaf, C. C. Gamze, M. Matej, O. Maria, and U. O. Aysegul, *Research on Chemical Intermediates*, **44**: 3325 (2018); doi:10.1007/s11164-018-3309-0
42. S. Thogiti, T. T. C. Thi, K. J. Yoon, Y. E. Joo, A. K. Soon, B. Y. Shin, L. S. Woo, and K. J. Hong, *Molecular Crystals and Liquid Crystals*, **620**, Iss. 1: 71 (2015); https://doi.org/10.1080/15421406.2015.1094870
43. S. Napisah, J. Aidah, J. Mohammad, and K. Anish, *Polymers*, **12**, Iss. 11: 2522 (2020); https://doi.org/10.3390/polym12112522
44. X. Zhang, J. Zhang, R. Wang, T. Zhu, and Z. Liu, *Chem. Phys. Chem.*, **5**, Iss. 7: 998 (2004); https://doi.org/10.1002/cphc.200301217
45. S. Z. Yao and M. T. Lee, *Materials*, **10**, Iss. 5: 555 (2017); doi:10.3390/ma10050555
46. S. Dandan, C. Peng, W. Tianyue, X. Bixia, J. Yongjian, L. Meicheng, L. Yaoyao, D. Sheng, H. Yue, L. Zhuohai, and M. J. Michel, *Nano Energy*, **23**: 122 (2016); https://doi.org/10.1016/j.nanoen.2016.03.006
47. K. Sharma, V. Sharma, and S. S. Sharma, *Nanoscale Res. Lett.*, **13**: 381 (2018); https://doi.org/10.1186/s11671-018-2760-6
48. P. Dhanasekaran and R. Marimuthu, *Frontiers in Energy Research*, **10**: 1 (2023); https://doi.org/10.3389/fenrg.2022.998038
49. D. Kumar, *Engineering Research Express*, **3**, Iss. 4: 042004 (2021); doi:10.1088/2631-8695/ac3b29
50. C. Yan, J. Wang, W. Kang, M. Cui, X. Wang, C. Y. Foo, and K. J. Chee, *Nanyang Technological University*, **26**, Iss. 13: 1950 (2014); https://doi.org/10.1002/adma.201470083
51. M. Mujahid, M. Ahmad and O. A. Al-Hartomy, *Optoelectronics and Advanced Materials-Rapid Communications*, **16**, Iss. 9–10: 464 (2022).
52. S. Mohanty, S. K. Nayak, B. S. Kaith, and S. Kalia, *Polymer Nanocomposites based on Inorganic and Organic Nanomaterials*, 89 (2015); https://doi.org/10.1002/9781119179108.ch4
53. Q. Zhou, J. Qiu, Y. Wang, M. Yu, J. Liu, and X. Zhang, *ACS Energy Letters*, **6**, Iss. 4: 1596 (2021); https://doi.org/10.1021/acsenergylett.1c00291

54. H. Monalisa and M. A. Kumar, *Journal of Materials Science: Materials in Electronics*, **30**: 4792 (2019); doi:10.1007/s10854-019-00773-8
55. C. Ziyi, X. Guoxin, H. Feng, W. Weiqi, G. Dan, and W. Wei, *Advanced Materials Interfaces*, **4**, Iss. 23: 1700998 (2017); https://doi.org/10.1002/admi.201700998
56. L. Jianneng, C. Dachang, A. Keegan, S. Qian, H. N. Graham, Z. Yang, S. Yipeng, L. Jing, L. Ruying, Z. Li, Z. Shangqian, L. Shigang, H. Huan, Z. Xiaoxing, S. C. Veer, and S. Xueliang, *Advanced Energy Materials*, **11**, Iss. 1: 2002455 (2021); https://doi.org/10.1002/aenm.202002455
57. J. C. R. Morales, D. M. López, M. G. Sánchez, J. C. Vázquez, C. Savaniud, and S. N. Savvina, *Energy & Environmental Science*, **3**, Iss. 11: 1670 (2010); https://doi.org/10.1039/C0EE00166J
58. Yiding Song, Nan Wang, Yuanhao Wang, Renyun Zhang, Hekan Olin, and Ya Yan, *Advanced Energy Materials*, **10**, Iss. 45: 2002756 (2020); https://doi.org/10.1002/aenm.202002756
59. S. P. Wulan, Y. D. Kusuma, and D. A. Handrini, *AIP Conference Proceedings*, **1755**, Iss. 1: 160003 (2016); doi:10.1063/1.4958596
60. N. Gokilamani, N. Muthukumarasamy, M. Thambidurai, A. Ranjitha, V. Dhayalan, T. S. Senthil, and R. Balasundaraprabhu, *Journal of Materials Science: Materials in Electronics*, **24**, Iss. 9: 3394 (2013); doi:10.1007/s10854-013-1261-8
61. A. Arunachalam, S. Govindan, and S. Vadivel, *Subramanian and Balasubramanian, Materials in Electronics*, **28**: 18455 (2017); doi:10.1007/s10854-017-7792-7
62. A. Brüger, G. Fafilek, and M. N. Spallart, *Solar Energy*, **205**: 74 (2020); https://doi.org/10.1016/j.solener.2020.05.035
63. H. Masuda, Y. Ohta, and M. Kitayama, *Journal of Materials Science and Chemical Engineering*, **7**, Iss. 02: 1 (2019); doi:10.4236/msce.2019.72001